Independent Joint Control Simulations on Adaptive Maneuvering of a Magnetotactic Bacterium via a Single Permanent Magnet

Ahmet Fatih Tabak[1*]

[1] Kadir Has University, Faculty of Engineering and Natural Sciences, Department of Mechatronics Engineering, Istanbul, Turkey (ORCID: 0000-0003-3311-6942)

Abstract

The use of micro-robotic systems in non-invasive medicine has been heavily promoted in the literature for the last decade. The studies usually focus on artificial or biohybrid microswimmers of various origins subject to the effect of an external electromagnetic field controlled by a computer. Although there exist several motion control studies shared to date, control of a bio-hybrid microswimmer has rarely been demonstrated employing an open kinematic chain, in detail. In this work, motion control of an isolated magnetotactic bacterium cell (*Magnetospirillum Gryphiswaldens*) is presented via a magnetic field actively positioned by an open kinematic chain. The cell is modeled with its complete environment to make it as realistic as possible along with the magnetic torque, which is induced by a single magnet attached at the end effector of a robotic arm, exerted on it for maneuvering control. The control is based on a proportional – integral – derivative (PID) gain scheme with adaptive integral gain to focus on a particular steady-state error with discontinuous reference signals. The control signal is transformed into pulse width modulation (PWM) signals to drive the motors articulating the joints of the open kinematic chain, the inverse kinematics of which is designed to be simple enough to achieve independent joint control. A numerical analysis of the coupled system is carried out in the time domain. The performance of the said motion control approach is investigated for each degree of freedom for the planar motion of the microswimmer. Simulations demonstrate a planar open kinematic chain is capable of control the gait of the microswimmer while following its trajectory near a planar boundary via independent joint control. Furthermore, simulations demonstrate that the effective magnetic inertia and the shear stress results in a small but certain lag in the motion control performance of the overall system.

Keywords: Microrobots, Motion Control, Bio-hybrid Systems.

Tek Mıknatıs aracığılı ile bir Manyetotaktik Bakterinin Adaptif Manevra Kontrolü için Bağımsız Eklem Kontrol Simulasyonları

Öz

Mikro robotik sistemlerin invaziv olmayan tıptaki muhtemel uygulamaları son on yıldır literatürde yoğun bir şekilde gösterilmektedir. Yayınlanan çalışmalar büyük oranda bilgisayar kontrollü bir harici elektromanyetik alan içerisinde hareket eden farklı tiplerdeki yapay veya biyo-hibrid mikro yüzücülerin performansına odaklanmıştır. Mikro yüzücülerin tamamen canlı doku içinde veya harici ortamlarda yüzme ve hareket kontrol performansı ile ilgili çalışmalar yaygındır, ancak biyo-hibrid bir mikro yüzücünün başka bir robot yardımı ile hareket kontrolü şu ana kadar literatürde hiç detaylı olarak gösterilmemiştir. Bu çalışmada, gerçek bir manyeto taktik bakteri hücresinin (*Magnetospirillum Gryphiswaldens*) belirli bir mesafeden hareket ve manevra kontrolünün simülasyonu yapılmıştır. Seçilen canlı hücrenin yüzme yönü, mıknatıs yerleştirilmiş bir robot kolunun hareketi ve bu mıknatısın manyetik alanı sonucu ortaya çıkan manyetik tork yardımı ile kontrol edilmektedir. Kontrol performansı, süreksiz fonsksiyon olarak tanımlanmış oryantasyon referansına karşın ortaya çıkan pozisyon takip hatasının oransal – integral – türev (PID) denetleyicisi yardımı ile minimize edilmesine dayanmaktadır. Ayrıca, integral katsayısı anlık hataya bağlı olarak değişecek şekilde, yani adaptif olarak, modellenmiştir. Tüm sistemin dinamik ve kinematik davranışı için nümerik çözümler zamana bağlı olarak gerçekleştirilmiştir. Hareket kontrol sisteminin performansı, mikro

* Corresponding Author: Kadir Has University, Faculty of Engineering and Natural Sciences, Department of Mechatronics Engineering, Istanbul, Turkey, ORCID: 0000-0003-3311-6942, ahmetfatih.tabak@bau.edu.tr

robotun düzlemsel hareketindeki her bir serbestlik derecesi için ayrı ayrı incelenmiştir. Simülasyon çalışmaları göstermektedir ki; bağımsız eklem kontrolü metodu ile hareket ettirilen düzlemsel bir robot kol, aynı anda canlı hücrenin düz bir katı yüzeyine yakın olarak hareketini takip ederken, yüzme yönünü tayin etmek için de başarılı bir şekilde kullanılabilir. Ayrıca, yapılan simülasyonlar, manyetik alandaki efektif atalet ve mikro robot üzerinde hissedilen sıvı direncinin kontrol reaksiyonunda küçük fakat hissedilir bir gecikmeye neden olduğuna işaret etmektedir.

1. Introduction

Medicine and robotics have been recently combining efforts towards a new type of surgical robot to achieve minimally invasive operations (François et al., 2019; Ceylan et al., 2017; Sitti et al., 2015; Nelson et al., 2010; Tabak, 2019; Singh et al., 2019; Soto and Chrostowski, 2018). Micro robotic systems designed for therapeutic operations often consists of a micron-sized end-effector and a much larger complex component responsible for visualization, decision making and energy supply (Dreyfus et al., 2005; Alapan et al., 2018; Medina-Sánchez et al., 2016; Nagai, et al. 2019). Therapeutic microswimmers, in the literature, are often controlled by electromagnetic fields of different origins such as magnetic resonance imaging (MRI), Helmholtz coils, and permanent magnets (Belharet et al., 2010; Tamaz et al., 2008; Khalil et al., 2017a; Servant et al., 2015; Wu et al., 2018; Ceylan et al., 2018). The complexity of the field and field gradients to achieve motion control diminish drastically when the microswimmer does not require external energy transmission (Ghosh and Fischer, 2009; Felfoul and Martel, 2013). This leads to simplification of the actuation system; however, the necessity of relatively larger workspace to accommodate living tissue, e.g. eyeball or spinal column of a human subject (Wu et al., 2019; Kummer et al., 2010; Fountain et al., 2010), poses yet another challenge.

The field should extend in all directions, however, at the expense of dedicated electronics and higher values of electric currents flowing through the coil wires followed by Joule heating and associated cooling efforts. Moreover, the density of the field decays with the cube of the distance (Kummer et al., 2010; Petruska and Abbott, 2013) limiting the boundaries of the workspace hence the spatial freedom of the microswimmer. This would also affect the geometric design of the microswimmer as well as the control law to the desired operation. There are two practical solutions to the problem of achieving the desired field over a relatively large area; namely employing stationary or mobile systems comprising of either electromagnetic coils or permanent magnets (Khalil et al., 2017a; Akçura et al., 2018). One of the simplest and the least energy-consuming methods is to employ a permanent magnet acting as an end-effector to an open kinematic chain, given the control, the law maintains a certain level of accuracy on the setpoint tracking. Such a system could be more practical for certain applications where strong magnetic fields are not necessary, i.e., the targeted tissue is close to the exterior of the organism. However, this method of approach is not well documented in the literature whereas there are ample data for other methods (François et al., 2019; Ceylan et al., 2017; Sitti et al., 2015; Nelson et al., 2010; Tabak, 2019; Singh et al., 2019; Soto and Chrostowski, 2018).

The proposed system simulated here is composed of an open kinematic chain and a microswimmer, magnetotactic bacteria species *Magnetospirillum Gryphiswaldens* (Khalil et al., 2013; 2017b). The open kinematic chain, i.e., the robotic arm, has a permanent magnet attached to it and the control law employs adaptive integral gain at each associated joint along with an independent proportional-integral-derivative (PID) control scheme. The robotic arm is controlled to follow the position of the microswimmer while the permanent magnet is utilized to change the heading of the microswimmer concerning an external time-dependent yaw-angle reference. The tuning parameters to the PID controller are found via numerical search over a cost function based on the setpoint tracking errors at the joints. The control signal is used to generate the necessary pulse width modulation (PWM) signals for the motors articulating the joints of the open kinematic chain. The inverse kinematics of the robotic system is selected to be simple enough to achieve independent joint control effortlessly. Furthermore, the said time-dependent yaw-angle reference signals are designed as discrete functions as to introduce additional non-linearity to the control signal dynamics to investigate its behavior with sudden discontinuities. The results of the numerical model demonstrate that the controller performs with an agreeable tracking error.

2. Theory and the Numerical Setup

2.1. The Geometric Arrangement of the Robotic System

The system consisting of two separate robots, i.e., the open kinematic chain and the untethered bacterium cell, could be modeled as one robotic arm. The selected open kinematic chain configuration has three degrees-of-freedom (DOF) with prismatic-prismatic-revolute (PPR) joint arrangements. The revolute joint holds the permanent magnet which controls the yaw-angle of the bacterium cell. The bacterium cell has one helical tail attached to its head and they are known to rotate in opposite directions. The cell is moving close to a flat solid boundary virtuously eliminating three of its six DOF. Figure 1 demonstrates the position and orientation of the two robots concerning each other. Figure 2 illustrates the additional three DOF based on the rigid-body motion of the bacterium cell and the orientation of the magnet and the microswimmer concerning each other.

Although there is no tactile contact between the magnet and the bacterium cell, a fictitious elastic link constituting three additional DOF could be modeled between the two systems. The Denavit-Hartenberg table, i.e., Table 1 (Spong and Vidyasagar, 1989), including the aforementioned fourth, fifth, and sixth DOF to the proposed systems should indicate all the necessary traverse and rotation steps along respective x- and z-axes as follows here. The three-DOF arm is articulated by the three links of the PPR arm. Each link has a dedicated actuator. The motion of the permanent magnet is confined to a plane and, as given in Figure 1, the first two links realize the

planar traverse of the third link. Furthermore, the third link houses and rotates the permanent magnet, thus changing the orientation of the magnetic field. It should be also noted that the Denavit-Hartenberg table dictates that the link has no length.

The angle between the permanent magnet and the microswimmer, i.e., the instantaneous misalignment, constitutes the fourth DOF. The actuator of the fourth link is the permanent magnet and the link itself can be considered as a magnetic link. The control law, as explained in *2.3 The Control Law*, is supposed to keep the said misalignment as small as possible during operation, i.e., steady-state error, through magnetic field orientation concerning the microswimmer along their z-axes as depicted in Figure 2. The selected magnetotactic bacteria species *Magnetospirillum Gryphiswaldens* (Khalil et al., 2013; 2017b) has magnetic crystals that react to the external magnetic field exerting a net torque leading to the rigid-body rotation, as explained in *2.2 Equation of Motion,* rendering this approach technically possible.

The last two DOF are functions of the position of the microswimmer in the lab frame, $x_{sw}(t)$, and $y_{sw}(t)$, and they are not subject to the control law; therefore, the overall system is underactuated. However, the joint variables of the aforementioned axes are written in the form of set-point tracking error (Spong and Vidyasagar, 1989) that can be considered as fictitious elastic deformation and will be directly used by the control law calculating the associated pulse-width-modulation (PWM) signals for the first two DOFs of the PPR arm.
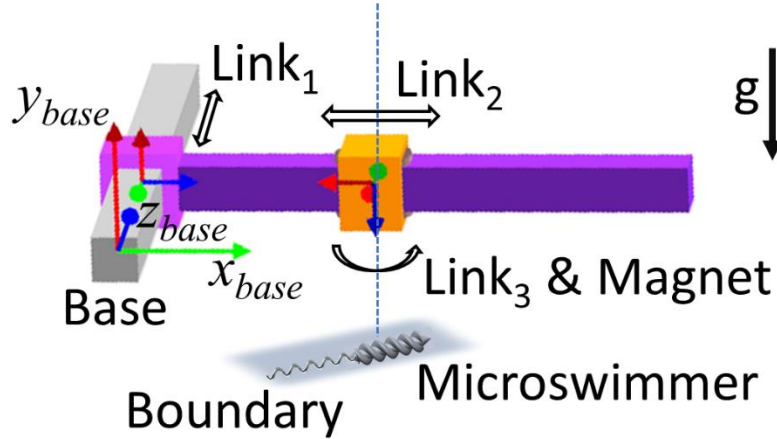
Figure 1:

The open kinematic chain with three DOFs and three joints in the order of prismatic-prismatic-revolute (PPR) as shown in the figure above and the microswimmer, i.e., single untethered magnetotactic bacterium cell swimming near a solid boundary constituting the last three DOFs to the overall system. The permanent magnet is the third link and it is embedded at the tip of the second link creating a concatenated structure. *The open kinematic chain is visualized with the help of RoboAnalyzer software (Othayoth et al., 2017).*

Table 1. Effective Denavit-Hartenberg (Spong and Vidyasagar, 1989) table for the entire system, i.e., open kinematic chain (PPR) and the magnetotactic bacterium (microswimmer).

Degrees-of-freedom	θ	d	a	α
#1	0	$d_1(t)$	0	$-\pi/2$
#2	$\pi/2$	$d_2(t)$	0	$-\pi/2$
#3	$\theta_3(t)$	0	0	0
#4	$\theta_4(t) = \theta_{sw\text{-}z}(t)$	d_4	0	π
#5	0	$d_5(t) = y_{sw}(t) - d_1(t)$	0	$\pi/2$
#6	$\pi/2$	$d_6(t) = x_{sw}(t) - d_2(t)$	0	$-\pi/2$
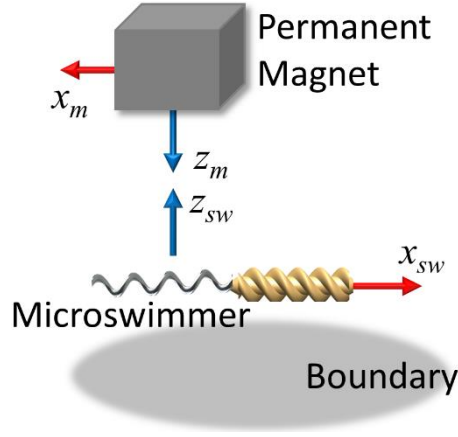
Figure 2:
The permanent magnet and the microswimmer, concerning each other's position and orientation, as in Figure 1. The fictitious link between the two is modeled employing the combined effect of the magnetic torque, constraint torque, and the adaptive control law of the choice.

2.2. The Equation of Motion

The governing equation for the equivalent robotic arm, based on the original Denavit-Hartenberg table and Euler-Lagrange modeling approach (Spong and Vidyasagar, 1989) including the dynamics of the electric motors attached to actively controlled joints, is as follows:

$$\ddot{q} = D^{-1}(q)\big(K_m I_m - r_m^{-1} T_{constraint} - C(q, \dot{q})\dot{q} - g(q)\big), \tag{1}$$

$$\dot{I}_m = L_m^{-1}(V_m - K_b \dot{q} - R_m I_m). \tag{2}$$

Here, $\mathbf{D}$, $\mathbf{C}$, $\mathbf{g}$, $\mathbf{K}_m$, $\mathbf{I}_m$, $\mathbf{r}_m$, $\mathbf{T}_{constraint}$, $\mathbf{L}_m$, $\mathbf{R}_m$, $\mathbf{V}_m$, and $\mathbf{K}_b$ denote the mass matrix, the Christoffel coefficient matrix, gravity force vector, torque constant matrix, motor current vector, joint reduction rate matrix, constraint vector for the joints (Raibert and Craig, 1981), motor inductance matrix, motor resistance vector, motor voltage vector, and electromotive force (EMF) matrix of the dedicated direct-current (DC) motors at the joints, respectively. Thus, two equations above capture the entire electromechanical behavior of the first three DOFs of the robotic system demonstrated in Figure 1. Furthermore, the vector q denotes the generalized coordinates such that $\mathbf{q} = [q_1\ q_2\ q_3]^T = [d_1\ d_2\ \theta_3]^T$. Moreover, the constraint effect deserves additional focus as it denotes the interaction, either physical or fictitious, of each ith link with its environment:

$$T_{i-\text{constraint}} = -sgn(q_i)b_d\dot{q}_i(sgn(q_i\dot{q}_i) > 0) - sgn(q_i)k_d(q_i - q_{lim})(q_i > q_{lim}), \tag{3}$$

with b_d and k_d signifying the damping constant and spring constant, respectively, of the joints under the influence of a contact force. This constraint torque also constitutes the fictitious elastic deformation of the fourth link. Here, one can obtain the accelerations at the first three joints using the aforementioned equations. Next, using the low Reynolds (Re) number assumption and resistive force theory (RFT) (Purcell, 1977; Keller and Rubinow, 1976; Tabak, 2018), the equation of motion for the last three DOFs are written as follows:

$$\begin{bmatrix} V_{\text{sw}} \\ \Omega_{\text{sw}} \end{bmatrix} = -(B_{head} + B_{tail})^{-1} \begin{bmatrix} F_p(t) + F_m(t) + F_g(t) + F_c(t) \\ T_p(t) + T_m(t) + T_g(t) + T_c(t) \end{bmatrix}, \tag{4}$$

$$\begin{bmatrix} F_p \\ T_p \end{bmatrix} = B_{tail} \begin{bmatrix} 0 \\ \Omega_{tail} \end{bmatrix}, \tag{5}$$

$$\begin{bmatrix} F_m \\ T_m \end{bmatrix} = \begin{bmatrix} (m \cdot \nabla)B_{mag-sw} \\ m \times B_{mag-sw} \end{bmatrix}, \tag{6}$$

$$\begin{bmatrix} \boldsymbol{F}_g \\ \boldsymbol{T}_g \end{bmatrix} = \begin{bmatrix} m_{eff}\boldsymbol{g}_{sw} \\ \boldsymbol{r}_{head} \times \boldsymbol{F}_g \end{bmatrix}, \tag{7}$$

$$\begin{bmatrix} \boldsymbol{F}_c \\ \boldsymbol{T}_c \end{bmatrix} = \begin{bmatrix} \left(k_c \begin{pmatrix} \delta \Leftarrow \delta < 0 \\ 0 \Leftarrow \delta \geq 0 \end{pmatrix} + b_c \begin{pmatrix} \frac{d\delta}{dt} \Leftarrow \frac{d\delta}{dt}< 0 \\ 0 \Leftarrow \frac{d\delta}{dt} \geq 0 \end{pmatrix} \right) \boldsymbol{n}_c \\ \boldsymbol{r}_c \times \boldsymbol{F}_c \end{bmatrix}. \tag{8}$$

Here, the resultant rigid-body velocity vector of the microswimmer, i.e., $[\mathbf{V}_{sw}\ \mathbf{\Omega}_{sw}]^{\mathrm{T}}$, is found with the respective accelerations assumed to be infinitesimal by the resistive force theory. The matrices $\mathbf{B}_{head}$ and $\mathbf{B}_{tail}$ are the viscous resistance matrices of head and tail to the microswimmer (Tabak, 2018), respectively. The fluid resistance is acting against the cumulative effect of propulsion, i.e., $[\mathbf{F}_p\ \mathbf{T}_p]^{\mathrm{T}}$, the field of the permanent magnet (Petruska and Abbott, 2013), i.e., $[\mathbf{F}_m\ \mathbf{T}_m]^{\mathrm{T}}$, gravity, i.e., $[\mathbf{F}_g\ \mathbf{T}_g]^{\mathrm{T}}$, and contact with the boundary, i.e., $[\mathbf{F}_c\ \mathbf{T}_c]^{\mathrm{T}}$, depicted in Figure 2 (Spong and Vidyasagar, 1989; Rengifo et al., 2009). The helical tail of the microswimmer is rotating with the angular velocity of $\mathbf{\Omega}_{tail} = [0\ 0\ \Omega_{\underline{z}}]^{\mathrm{T}}$. The magnetic field felt by the microswimmer in its frame of reference, i.e., $\mathbf{B}_{mag\text{-}sw}$, exerts the influence on the dipole moment of its head, i.e., $\mathbf{m}$, as such the swimming direction can be altered at will. In the meantime, gravitational attraction felt by the microswimmer, again, in its frame of reference, i.e., $\mathbf{g}_{sw}$, pulls the effective mass, after the buoyancy is included, towards the boundary beneath. The boundary exerts a reaction force at the instance of contact and it has conditional components, i.e., spring, k_c, and damping, b_c, depending on the penetration of the microswimmer, δ, in meters or radians. One should note that the directions of the contact force and torque vectors depend on the surface normal at the contact, i.e., $\mathbf{n}_c$, and the position vector of point of contact concerning the center of mass of the microswimmer, i.e., $\mathbf{r}_c$. Similarly, $\mathbf{r}_{head}$ signifies the position to the mass center of the head relative to the center of mass of the microswimmer.

2.3. The Control Law

The PID control is applied to all DC-motors, separately. The inverse kinematics of the robotic system represented is relatively easy due to the presence of prismatic joints: The first three DOFs of the robot is the mirror image of the last three DOFs rendering x, y, and z-axis kinematics virtually independent of each other. Thus, the control effort is also greatly simplified. The PID controller used in this study is inspired by the works of (Denai et al., 1990; Lugmair et al., 2003). The aforementioned control law for the first three DOFs, i.e., of the system is given as:

$$\tau_{\{x,y,z\}} = K_{p-\{x,y,z\}}e_{\{x,y,z\}}(t) + \int K_{i-\{x,y,z\}}e_{\{x,y,z\}}(t)dt + K_{d-\{x,y,z\}}\dot{e}_{\{x,y,z\}}(t), \tag{9}$$

$$K_{i-\{x,y,z\}} = \frac{1}{((K_{ia-\{x,y,z\}}e_{\{x,y,z\}}(t))^{0.5}+1)}. \tag{10}$$

Here, the coefficients K_p, K_i, and K_d are the coefficients of proportional, integral, and derivative gains, respectively. The integral gain is adaptive and tuned online with the current error in set-point tracking as depicted above. Furthermore, the control law applied on each joint is computed based on the instantaneous setpoint tracking error, $e(t)$, and the error is defined at each frame and associated axis, as depicted in Figure 1 and Figure 2, in the following form:

$$e_y(t) = d_{x-sw}(t) - d_{y-PPR}(t), \tag{11}$$

$$e_x(t) = d_{y-sw}(t) - d_{x-PPR}(t), \tag{12}$$

$$e_z(t) = \theta_z^{ref}(t) - \theta_{z-sw}(t). \tag{13}$$

This control law, in compliment to the equation of motion set, explained before, ensures bilateral control of the two distinct robots which will act as one open kinematic chain as explained here: first two joints of the PPR arm will be responsible for tracking the microswimmer along xy-plane whereas the third joint will exert the magnetic torque via the permanent magnet to change the heading of the micro simmer as per the yaw-reference provided by a higher-level control, e.g., an operator or an automated gait controller. Also, the voltage applied to the DC-motors are in the form of the PWM signal that is generated as follows:

$$\chi_i = |\tau_i|/\tau_{i-max}, \tag{14}$$

$$\psi_i = t/f_{\text{PWM}} - floor(t/f_{\text{PWM}}), \tag{15}$$

and thus

$$\text{PWM} = sgn(\tau_i)\begin{cases}1 \Leftarrow \psi_i < \chi_i \\ 0 \Leftarrow \psi_i \geq \chi_i\end{cases}. \tag{16}$$

Here, the PWM signal is supposed to be amplified to the actual voltage rating of the DC-motor to simulate its dynamics properly.

3. Results

The following results are obtained for *M. Gryphiswaldense* species (Khalil et al., 2017b) as the microswimmer moving near a plane boundary constituting the last three DOFs, N52-grade Neodymium permanent magnet (Dong et al., 2019) $0.02 \times 0.02 \times 0.02 \text{ m}^3$ of volume attached at the third axis, and "EC 45 Flat" (Maxon Group, 2019) DC-motors at each joint of the PPR arm. The PPR arm is designed to be made out of aluminum and the first two joints are modeled as rectangular prisms with dimensions of 5 cm × 5 cm × 30 cm. The last link is comprised of the permanent magnet and it is embedded at the tip of the second link creating a concatenated structure. Moreover, the dimension 30 cm denotes the maximum extent of the prismatic joints. The computations are carried out using "GNU Octave" (Eaton et al., 2019) and forward integration in time-domain (Shampine and Gordon, 1975) with an openSUSE Linux machine running on 64-bit i7 CPU and 32 Gb RAM.

Figure 3, Figure 4, Figure 5, and Figure 6 demonstrate the performance and behavior of the discussed system under the said control law. The external time-dependent yaw-angle reference, i.e., $\theta_z^{ref}(t)$, imposed on the gait of the microswimmer is set as a discontinuous function of the form:

$$\theta_z^{ref}(t) = \begin{cases}0 \Leftarrow t < 0.25 \\ (\pi/36)(t - 0.25) \Leftarrow t \geq 0.25\end{cases}, \tag{17}$$

and the total simulation time is set as 1.25 seconds. The PID coefficient set used is $K_{p-x} = 7.5741$, $K_{ia-x} = 0.5050$, $K_{d-x} = 0.0101$, $K_{p-y} = 7.5745$, $K_{ia-y} = 0.5049$, $K_{d-y} = 0.0097$, $K_{p-z} = 0.0101$, $K_{ia-z} = 0.0020$, $K_{d-z} = 0$ for this simulation study.

The associated set-point tracking performance is given here. It has been observed that the maximum tracking error for the first two joints of the PRR arm is around 20 μm as given in Figure 3 and Figure 4. This error is larger than the size of the designated bacterium species, i.e., ~10 μm head and single helical tail in total (Khalil et al., 2017b); however, the maximum time-dependent tracking error to the yaw-angle reference is found to be 2×10^{-2} rad, successfully. Although the results are fairly good to demonstrate the reaction of the system to the setpoint error and the adaptive control input, better results could arguably be achieved if an optimization study is carried out on the control parameter tuning especially on the x- and y-axes of the open kinematic chain. It could also be argued that the errors are in acceptable range as long as the swimming direction of the microswimmer is controlled with high accuracy.

Finally, the PWM signal generated for the DC-motor at the third joint (see Table 1 and Figure 1) is presented in Figure 6 to demonstrate the input to the DC-motor and its relationship with the observable stead-state oscillation in Figure 2. The reason to that is the inherent trajectory of the microrobot as it is following a helical path with wobbling motion in all axes (Lauga et al, 2006; Constantino et al, 2016) and the control performance is trying to compensate for that.
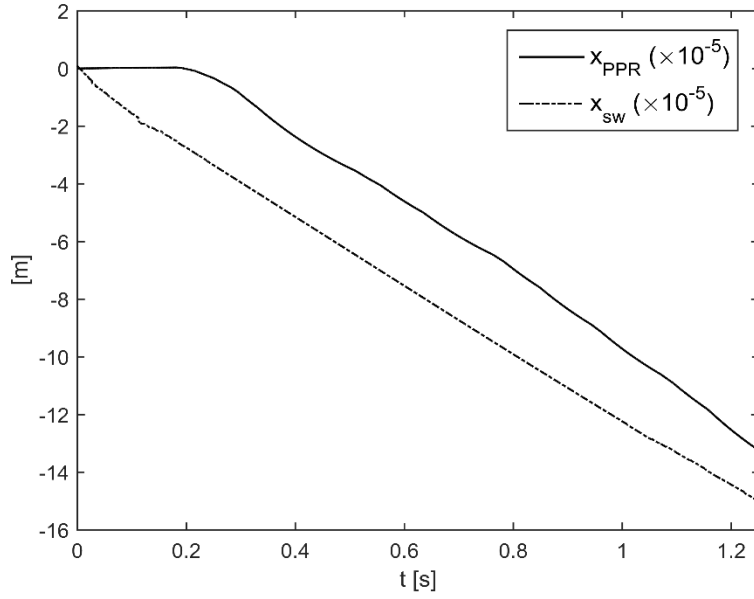
Figure 3:
Performance of the PID controller on the position of the second joint of the PPR arm (Figure 1). The reference is $x_{sw}(t)$, depicted by the broken line; the joint variable is $x_{PPR}(t)$, depicted by the continuous line.
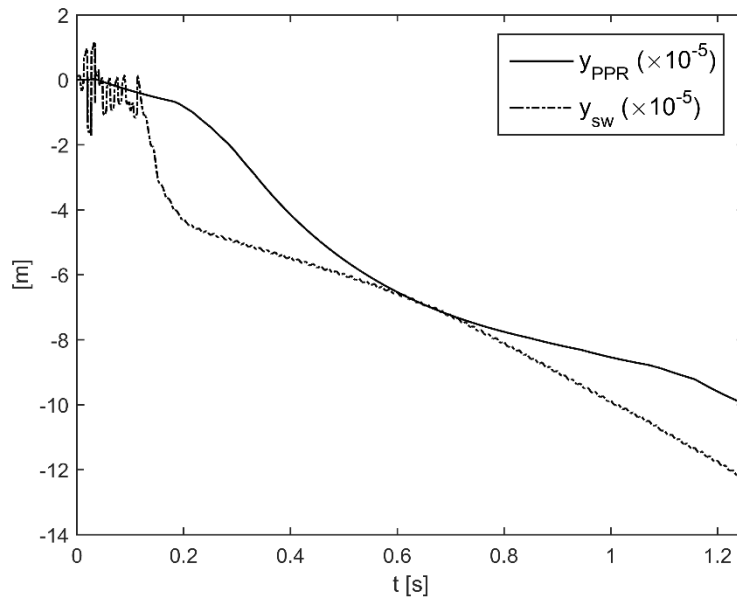
Figure 4:
Performance of the PID controller on the position of the first joint of the PPR arm (Figure 1). The reference is $y_{sw}(t)$, depicted by the broken line; the joint variable is $y_{PPR}(t)$), depicted by the continuous line.
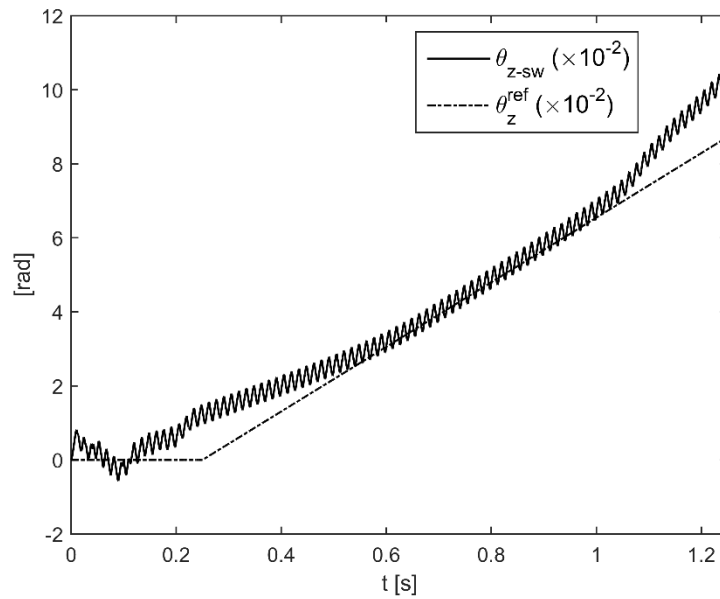
Figure 5:
Performance of the PID controller on the yaw-angle of the microswimmer (Figure 1 and Figure 2). The external reference is $\theta_z^{ref}(t)$, depicted by the broken line; the yaw-angle of the microswimmer is $\theta_{z-sw}(t)$), depicted by the continuous line.
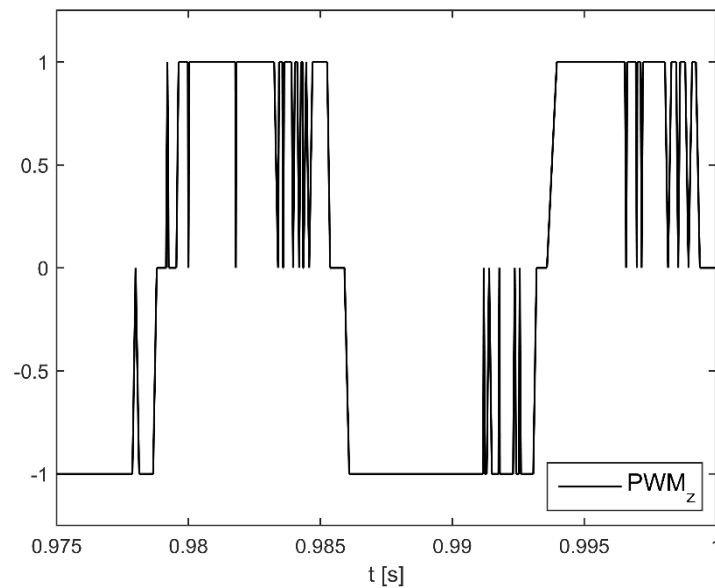
Figure 6:
Zoomed-in performance of the PID controller along the z-axis for the yaw-angle reference, $\theta_z^{ref}(t)$, under the influence of the general rigid-body motion of the microswimmer.

4. Discussion

The potential of bacteria as robotic agents for therapeutic operations has been discussed at great length in the last decade. The proposed method of control usually incorporates a very cumbersome electromagnetic system to include the necessary magnetic field. On the other hand, if the tissue is not deep in the organism, a relatively weaker magnetic field can be employed for micro-motion control studies. In this work, a method of position control study for the bacterium-based microswimmer is presented via an external magnetic field of a single permanent magnet to demonstrate the possibility. The mathematical model, thus the physical system, can further be expanded into a more complex arrangement by adding additional arms and magnets.

The microswimmer is dynamically decoupled from the overall robotic scheme it is incorporated. The aforementioned decoupling made it possible to perform set point tracking control at the axis of the end-effector given an external time-dependent reference. The effortless inverse kinematics and absence of apparent singularities of the system renders the control law simple; however, this does not

guarantee high accuracy for the setpoint tracking control on the former joints. The magnet is large enough to generate the field to exert sufficient z-torque on the microswimmer and the microswimmer can react to the magnetic stimuli fairly fast enough. It should be noted that the PPR arm, in its entirety, is bulky and heavy as opposed to the microswimmer; however, selected DC-motors proved to be agile and strong enough to handle the simulated control task. Nevertheless, one should also acknowledge the control law and the tuning coefficients employed in this study fell short on tracking the rigid-body motion along the xy-plane. Furthermore, the reference signals are discretized to introduce instantaneous nonlinearity to the error input to the PID controller, and it is observed that the said effect could not be captured to the fullest due to the reaction time of the magnetotactic. This behavior could indicate that an inherent delay in the system due to the magnetic inertia as well as shear friction acting on the surface of the bacterium cell, and should further be studied for more complex control signals in the future. The tracking performance along the z-axis, however, is arguably sufficient to follow the reference of $\theta_z^{ref}(t)$ for a relatively long time interval although a small deviation is observed towards the end of the simulation.

Finally, it can be argued that this system should be able to follow the microswimmer within a workspace limited by the farthest extent of the prismatic joints. This ensures autonomous gait control over a distance much longer than the body length of a bacterium cell. It can also be deduced that such a system can be used to control the center of mass of magnetotactic bacteria swarms in the future studies given the permanent magnet is large enough to generate the necessary field in a wider stretch. Such a robotic design could be easily fitted for operations in the living tissue and the magnet could also be much larger to obtain the field to penetrate deep in the tissue of interest. Further in vivo simulation studies for various tissue types should be conducted to ascertain the abilities and limitations to the proposed control method under different physiological conditions. It is worth mentioning that different biological fluids would introduce additional nonlinear effects via non-Newtonian behavior in which case one should consider using the proper viscosity with the measured property of shear-thinning or shear-thickening.

Reference

1. François, Q., André, A., Duplat, B., Haliyo, S., & Régnier, S. (2019) Tracking systems for intracranial medical devices: a review, *Medical Devices and Sensors*, 2(2), e10033. https://doi.org/10.1002/mds3.10033
2. Ceylan, H., Giltinan, J., Kozielski, K., & Sitti, M. (2017) Mobile microrobots for bioengineering applications, *Lab on a Chip*, 17(10), 1705-1724. https://doi.org/10.1039/C7LC00064B
3. Sitti, M., Ceylan, H., Hu, W., Giltinan, J., Turan, M., Yim, S., & Diller, E. (2015) Biomedical applications of untethered mobile milli/microrobots, *Proceedings of the IEEE*, 103(2), 205-224. https://doi.org/10.1109/JPROC.2014.2385105
4. Nelson, B.J., Kaliakatsos, I.K., & Abbott, J.J. (2010) Microrobots for minimally invasive medicine, *Annual Review of Biomedical Engineering*, 12, 55-85. https://doi.org/10.1146/annurev-bioeng-010510-103409
5. Tabak, A.F. (2019) Bioinspired and biomimetic micro-robotics for therapeutic applications, in Handbook of Biomechatronics, 1. Ed., J. Segil, Eds., Academic Press, U.K. https://doi.org/10.1016/b978-0-12-812539-7.00010-6
6. Singh, A.V., Ansari, M.H.D., Laux, P., & Luch, A., (2019) Micronanorobots: important considerations when developing novel drug delivery platforms, *Expert Opinion on Drug Delivery*, 16(11), 1259-1275. https://doi.org/10.1080/17425247.2019.1676228
7. Soto, F., & Chrostowski, R. (2018) Frontiers of medical micro/nanorobotics: in *vivo* applications and commercialization perspectives toward clinical uses, *Frontiers in Bioengineering and Biotechnology*, 6, 170. https://doi.org/10.3389/fbioe.2018.00170
8. Dreyfus, R., Baudry, J., Roper, M.L., Fermigier, M., Stone, H.A., & Bibette, J. (2005) Microscopic artificial swimmers, *Nature*, 437, 862-865. https://doi.org/10.1038/nature04090
9. Alapan, Y., Yasa, O., Schauer, O., Giltinan, J., Tabak, A.F., Sourjik, V., & Sitti, M. (2018) Soft erythrocyte-based bacterial microswimmers for cargo delivery, *Science Robotics*, 3(17), eaar4423. https://doi.org/10.1126/scirobotics.aar4423
10. Medina-Sánchez, M., Schwarz, L., Meyer, A.K., Hebenstreit, F., & Schmidt, O.G. (2016) Cellular Cargo Delivery: toward assisted fertilization by sperm-carrying micromotors, *Nano Letters*, 16(1), 555-561. https://doi.org/10.1021/acs.nanolett.5b04221
11. Nagai, M., Hirano, T., & Shibata, T. (2019) Phototactic algae-driven unidirectional transport of submillimeter-sized cargo in a microchannel, *Micromachines*, vol. 10(2), 130. https://doi.org/10.3390/mi10020130
12. Belharet, K., Folio, D., & Ferreira, A. (2010) Endovascular navigation of a ferromagnetic microrobot using MRI-based predictive control, *IEEE/RSJ International Conference on Intelligent Robots and Systems*, Taipei, Taiwan, 2804-2809. https://doi.org/10.1109/IROS.2010.5650803
13. Tamaz, S., Gourdeau, R., Chanu, A., Mathieu, J.-B., & Martel, S. (2008) Real-time MRI-based control of a ferromagnetic core for endovascular navigation, *IEEE Transactions on Bio-Medical Engineering*, 55(7), 1854-1863. https://doi.org/10.1109/TBME.2008.919720
14. Khalil, I.S.M., Alfar, A., Tabak, A.F., Klingner, A., Stramigioli, S., & Sitti, M. (2017a) Positioning of drug carriers using permanent magnet-based robotic system in three-dimensional space, *IEEE/ASME International Conference on Advanced Intelligent Mechatronics*, Munich, Germany, 1117-1122. https://doi.org/10.1109/AIM.2017.8014168
15. Servant, A., Qiu, F., Mazza, M., Kostarelos, K., & Nelson, B.J. (2015) Controlled in vivo swimming of a swarm of bacteria-like microrobotic flagella, *Advanced Materials*, 27(19), 2981-2988. https://doi.org/10.1002/adma.201404444
16. Wu, Z., Troll, J., Jeong, H.-H., Wei, Q., Stang, M., Ziemssen, F., Wang, Z., Dong, M., Schnichels, S., Qui, T., & Fischer, P. (2018) A swarm of slippery micropropellers penetrates the vitreous body of the eye, *Science Advances*, vol. 4(11), eaat4388. https://doi.org/10.1126/sciadv.aat4388
17. Ceylan, H., Yasa, I.C., Yasa, O., Tabak, A.F., Giltinan J., Sitti, M. (2018) 3D-printed biodegradable microswimmer for drug delivery and targeted cell labeling, *bioRxiv*, 1, 379024. https://doi.org/10.1101/379024
18. Ghosh, A., & Fischer, P. (2009) Controlled propulsion of artificial magnetic nanostructured propellers, *Nano Letters*, 9(6), 2243-2245. https://doi.org/10.1021/nl900186w

19. Felfoul, O., & Martel, S. (2013) Assessment of navigation control strategy for magnetotactic bacteria in microchannel: toward targeting solid tumours, *Biomedical Microdevices*, 15(6), 1015-1024. https://doi.org/10.1007/s10544-013-9794-4

20. Kummer, M.P., Abbott, J.J., Kratochvil, B.E., Borer, R., Sengul, A., & Nelson, B.J. (2010) OctoMag: an electromagnetic system for 5-dof wireless micromanipulation, *IEEE Transactions on Robotics*, 26(6), 1006-1017. https://doi.org/10.1109/TRO.2010.2073030

21. Fountain, T.W.R., Kailat, P.V., Abbott, J.J., (2010) Wireless control of magnetic helical microrobots using a rotating-permanent-magnet manipulator, *International Conference on IEEE Robotics and Automation*, Anchorage, AK, USA, 576-581. https://doi.org/10.1109/ROBOT.2010.5509245

22. Petruska, A.J., & Abbott, J.J. (2013) Optimal permanent-magnet geometries for dipole field approximation, *IEEE Transactions on Magnetics*, 49(2), 811–819. https://doi.org/10.1109/TMAG.2012.2205014

23. Akçura, N., Çetin, L., Kahveci, A., Alasli, A.K., Can, F.C., & Tamer, Ö. (2018) Guided motion control methodology for microrobots, *6th International Conference on Control Engineering & Information Technology*, Istanbul, Turkey. https://doi.org/10.1109/CEIT.2018.8751803

24. Khalil, I.S.M., Pichel, M.P., Abelmann, L., & Misra, S., (2013) Closed-loop control of magnetotactic bacteria, *International Journal of Robotics Research*, 32(6), 637-649. https://doi.org/10.1177/0278364913479412

25. Khalil, I.S.M., Tabak, A.F., Hageman, T., Ewis, M., Pichel, M., Mitwally, M.E., El-Din, N.S., Abelmann, L., & Sitti, M. (2017b) Near-surface effects on the controlled motion of magnetotactic bacteria, *IEEE International Conference on Robotics and Automation*, Singapore, 5976-5982. https://doi.org/10.1109/ICRA.2017.7989705

26. Spong, M.W., & Vidyasagar, M. (1989) Robot Dynamics and Control. John Wiley and Sons, Inc., New Jersey.

27. Othayoth, R.S., Chittawadigi, R.G., Joshi, R.P., & Saha, S.K. (2017) Robot kinematics made easy using RoboAnalyzer software, *Computer Applications in Engineering Education*, 25(5), 669-680. https://doi.org/10.1002/cae.21828

28. Raibert, M.H., & Craig, J.J. (1981) Hybrid position/force control of manipulators, *Journal of Dynamic Systems, Measurement, and Control*, 102, 126-133. https://doi.org/10.1115/1.3139652

29. Purcell, E.M. (1977) Life at low Reynolds number, *American Journal of Physics*, 45(1), 3-11, https://doi.org/10.1119/1.10903

30. Keller, J.B., & Rubinow, S.I. (1976) Swimming of flagellated microorganisms, *Biophysical Journal*, 16(2), 151-170. https://doi.org/10.1016/s0006-3495(76)85672-x

31. Tabak, A.F. (2018) Hydrodynamic impedance of bacteria and bacteria-inspired micro-swimmers: a new strategy to predict power consumption of swimming micro-robots for real-time applications, *Advanced Theory and Simulations*, 1(4), 1700013. https://doi.org/10.1002/adts.201700013

32. Rengifo, C., Aoustin, Y., Chevallereau, C., & Plestan, F. (2009) A penalty-based approach for contact forces computation in bipedal robots, *IEEE-RAS International Conference on Humanoid Robots*, Paris, France, 121-127. https://doi.org/10.1109/ICHR.2009.5379590

33. M. Denai, M., Linkens, D.A., Asbury, A.J., & Gray, W.M. (1990) Self tuning PID control of atracurium-induced muscle relaxation in surgical patients, *IEE Proceedings D – Control Theory and Applications*, 137(5), 261-272. https://doi.org/10.1049/ip-d.1990.0032

34. Lugmair, M., Froriep, R., Kuplent, F., & Langhans, L. (2003) Tempo beim laser im griff, *F&M Elektronik Jahrgang*, 111(5), 32-35.

35. Dong, F., Huang, Z., Qiu, D., Hao, L., Wu, W., & Jin, Z. (2019) Design and analysis of a small-scale linear propulsion system for maglev applications (1) – the overall design process, *IEEE Transactions on Applied Superconductivity*, 29(2), 5201005. https://doi.org/10.1109/TASC.2019.2895312

36. Maxon Group (2019) EC 45 flat Ø42.8 mm, brushless, 70 Watt, Maxon Catalogue Page. Retrieved from WWW https://www.maxongroup.com/maxon/view/product/397172 on 10.01.2019.

37. Eaton, J.W., Bateman, D., Hauberg, S., & Wehbring, R. (2019) GNU Octave version 5.1.0 manual: a high level interactive language for numerical computations.

38. Shampine, L.F., & Gordon, M.K. (1975) Computer Solution of Ordinary Differential Equations, W. H. Freeman and Company, San Francisco.

39. Lauga, E., DiLuzio, W.R., Whitesides, G.M., & Stone, H.A. (2006) Swimming in circles: Motion of bacteria in near solid boundaries, *Biophysical Journal*, 90, 400-412. https://doi.org/10.1529/biophysj.105.069401

40. Constantino, M.A., Jabbarzadeh, M., Fu, H.C., Bansil, R. (2016) Helical and rod-shaped bacteria swim in helical trajectories with little additional propulsion from helical shape, *Science Advances*, 2(11), e1601661. https://doi.org/10.1126/sciadv.1601661